Charge-exchange losses of beam ions in MAST Upgrade: experiments and modelling

OPEN ACCESS
IOP Publishing
Plasma Physics and Controlled Fusion
Plasma Phys. Control. Fusion **67** (2025) 055039 (18pp)
https://doi.org/10.1088/1361-6587/adcae8

Charge-exchange losses of beam ions in MAST Upgrade: experiments and modelling

P Ollus[1,*], T Kurki-Suonio[1], J Lovell[2], K G McClements[3], C A Michael[4], A Snicker[1,5], the MAST-U team[6] and the EUROfusion Tokamak Exploitation team[7]

[1] Department of Applied Physics, Aalto University, PO Box 11100, 00076 Aalto, Finland
[2] Oak Ridge National Laboratory, Oak Ridge, TN 37831, United States of America
[3] UKAEA (United Kingdom Atomic Energy Authority), Culham Campus, Abingdon, Oxfordshire OX14 3DB, United Kingdom
[4] Department of Physics and Astronomy, University of California—Los Angeles, Los Angeles, CA 90095-7099, United States of America
[5] VTT Technical Research Centre of Finland, Espoo, FI-02044 VTT, Finland

E-mail: patrik.ollus@aalto.fi

Received 15 August 2024, revised 13 March 2025
Accepted for publication 9 April 2025
Published 7 May 2025

Abstract

Dedicated experiments were performed on MAST Upgrade to study beam-ion losses caused by charge exchange (CX) with edge neutrals. The fuelling was switched from the high-field side to the low-field side mid-discharge. Direct measurements suggest a strong increase in the neutral density around the plasma and a decrease in the beam-ion density, which is qualitatively explained by CX losses. Measurements by a resistive bolometer have suggested particle bombardment during neutral beam injection, providing a unique opportunity to separate CX from other loss mechanisms. To verify and quantify CX losses, the orbit-following code ASCOT, which accounts both for CX neutralization and reionization, was used to simulate beam-particle power loads on the bolometer. Simulations reproduce measured bolometer power loads during high-field-side fuelling, verifying CX losses of approximately 10% of the off-axis beam power. Toroidally symmetric simulations overestimate power loads on the bolometer during low-field-side fuelling, which is explained by toroidal asymmetry in the neutral density distribution, as is demonstrated by toroidally asymmetric simulations. Results suggest significantly higher CX losses during low-field-side fuelling, up to about 50% of off-axis beam power.

[6] See Harrison *et al* (https://doi.org/10.1088/1741-4326/ab121c) for the MAST-U team.
[7] See Joffrin *et al* (https://doi.org/10.1088/1741-4326/ad2be4) for the EUROfusion Tokamak Exploitation team.
[*] Author to whom any correspondence should be addressed.

Keywords: fast ions, charge exchange, neutral density, toroidal asymmetry, MAST Upgrade, bolometer, ASCOT

1. Introduction

Fast ions in magnetically confined fusion plasmas can be transported and lost due to charge-exchange reactions with background neutrals, which causes, for example, loss of heating power [1–14]. In large conventional tokamaks, such as the future reactor ITER, the process is expected to have limited impact because of the large size of the plasma. Spherical tokamaks are particularly susceptible to fast-ion CX because of their compact geometry.

Experiments and modelling have indicated that significant losses of fast ions from neutral beam injection (beam ions) have been caused by CX reactions with edge neutrals in the Mega Amp Spherical Tokamak (MAST) and its successor MAST Upgrade (MAST-U) [7, 10, 13, 15]. Moreover, power balance calculations for MAST-U and the conventional tokamak JET have indicated beam-energy deficits that could be partially explained by CX losses [16, 17]. The observations of beam-ion CX losses in the 1st experimental campaign of MAST-U (MU01) motivated dedicated experiments in the 2nd and 3rd experimental campaigns of the device (MU02 and MU03) [18]. In these experiments, the fuelling was switched from the high-field side (HFS) to the low-field side (LFS), which was expected to increase the density of neutrals in the scrape-off layer (SOL) and plasma edge on the LFS. Previous work on MAST-U has shown that, since beam ions in the compact geometry orbit close to the LFS separatrix and have large gyroradii that reach far into the LFS SOL, most of the CX neutralizations that cause losses occur in the LFS SOL [10, 13]. Moreover, because the double-null shape of a typical MAST-U plasma separates the HFS and LFS SOLs completely, the difference between HFS and LFS fuelling may be pronounced. Goals of the present work included verifying that significant CX losses of beam ions occur in MAST-U in its current configuration, identifying plasma scenarios where CX losses should be expected, and quantifying CX losses of beam power, while accounting for reionization.

A range of fast-ion diagnostics was employed to measure the effects of the fuelling switch: a fast-ion deuterium-alpha (FIDA) [19, 20] system, a solid-state neutral-particle analyzer (SSNPA) [21] as well as a fission chamber [22] and a neutron camera [23], both of which measure neutron emission. To complement the direct measurements, interpretive modelling was performed using the transport code TRANSP [24, 25]. The direct measurements suggest a decrease in the beam-ion density that is qualitatively consistent with CX losses, but it is difficult to ascertain the true underlying mechanisms and quantify them. Measurements from a resistive bolometer have suggested particle bombardment caused by CX losses of beam ions [15], providing a unique opportunity to separate CX from other loss mechanisms. To verify and quantify CX losses, the fast-ion orbit-following code ASCOT (5th version) [26–28] was used to perform modelling tailored for comparison to the bolometer. The ASCOT CX model includes both the neutralization of a fast ion through CX with a background neutral, and the possible reionization of the resulting fast CX neutral, whose ballistic trajectory is followed [10, 13].

The rest of this article is organized as follows. Direct measurements and TRANSP modelling, with a focus on the fuelling switch, are presented in section 2. The quantitative investigation of CX losses through comparison of measured and ASCOT-simulated bolometer power loads is reported in section 3, with considerations of toroidal asymmetry in sections 3.2 and 3.5. Results are summarized and their implications discussed in section 4.

2. Switching from HFS to LFS fuelling

2.1. Direct measurements

In experiments dedicated to studying beam-ion CX, three double-null L-mode (low-confinement mode) plasma discharges (46 735, 49 447 and 49 452) were performed where the plasma fuelling (gas of deuterium molecules) was switched from HFS to LFS valves mid-discharge. This was intended to introduce additional background neutrals into the LFS SOL and plasma edge, thus increasing CX losses. To get a strong effect, particularly strong LFS fuelling was used, a flow rate of about $4.6 \cdot 10^{21}$ molecules s^{-1} (error margins of $\pm 10\%$ are assumed for flow rates). The average flow rate used in LFS fuelling at 0.3 s in LFS-fuelled discharges in MU01–MU03 was $2.1 \cdot 10^{21}$ molecules s^{-1}. Figure 1 gives an overview of the three discharges analyzed in this article, showing plasma current, line-integrated electron density, core electron temperature and neutral-beam power. Only the 'off-axis' beam, which injects horizontally 65 cm above the geometric midplane ($\rho_p \approx 0.8$, see figure 6), was used during times of primary interest, because particles from the off-axis beam are ionized closer to the edge and, therefore, are more susceptible to CX. In discharge 46735, the 'on-axis' beam, which injects horizontally in the geometric midplane, was turned on 100 ms after the fuelling switch, which led to a violent disruption at 300 ms after the fuelling switch.

Another reason not to use the on-axis beam was to avoid inducing magnetohydrodynamic (MHD) instabilities that would make it more difficult to study the effects of CX on beam ions. Figure 2 shows a spectrogram based on measurements by Mirnov coils [29] of discharge 49 452, which is representative of all three discharges. Comparing to spectrograms of discharges where the on-axis beam was used, where fast-ion instabilities typically cause structures to appear at frequencies of around 80 kHz, figure 2 shows no evidence of fast-ion instabilities. The structures that appear after 0.3 s at around

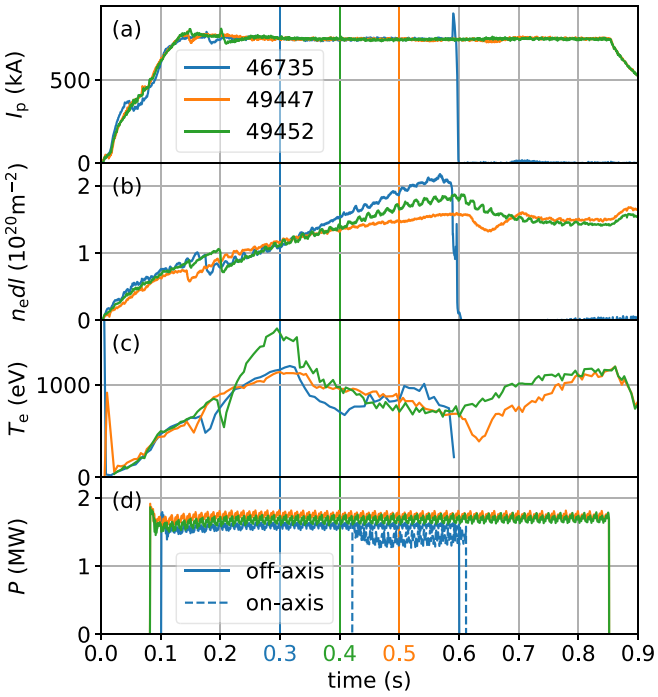

Figure 1. Plasma current (I_p) (a), line-integrated electron density $n_e dl$ (b), core electron temperature (T_e) (c) and neutral-beam power (P) (d) in discharges 46 735, 49 447 and 49 452. Fuelling switch times for the different discharges are indicated by colour-coding of x-axis tick labels and gridlines.

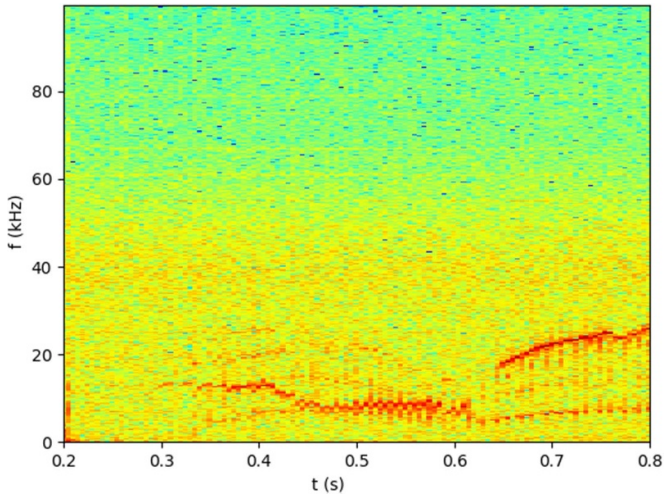

Figure 2. Spectrogram based on measurements by Mirnov coils of discharge 49 452 (t = time, f = frequency).

10 kHz look like pure MHD instabilities, most likely neoclassical tearing modes, which are expected to affect fast ions only weakly or not at all.

In discharge 46 735, the fuelling switch was programmed to occur at the time 0.30 s, as indicated in figure 1, and the LFS fuelling was kept on until the discharge disrupted at 0.60 s. A single midplane LFS fuelling valve was used, the valve in the toroidal sector 9. This valve and other relevant components are indicated in a top–down illustration of MAST-U in figure 3 to aid in describing the experiments and discussing the results. In

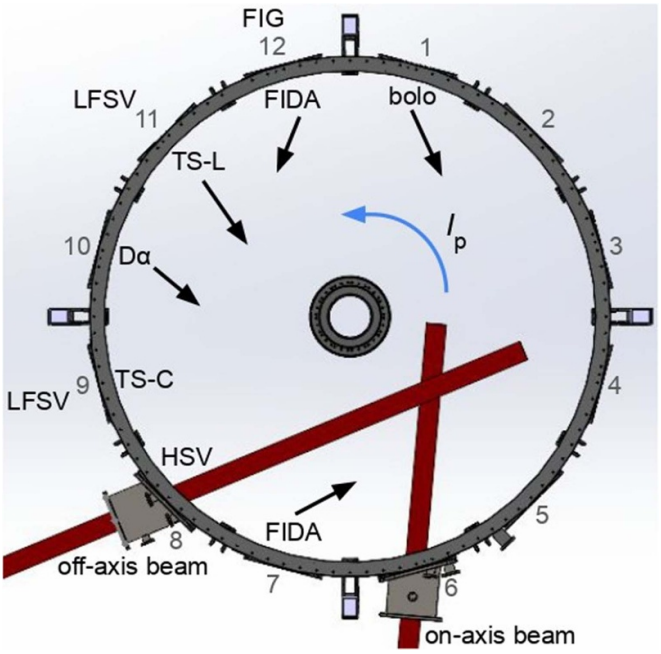

Figure 3. Top–down illustration of MAST-U, showing the beam lines and the approximate toroidal locations of the following relevant components: the two LFS fuelling valves (LFSV), the D-alpha diagnostic (Dα), the fast ion gauge (FIG), the two FIDA views, the Thomson scattering laser (TS-L) and collection system (TS-C), the high-speed-video camera (HSV), and the counter-beam bolometer (bolo). The number designations (1–12) for the toroidal sectors are indicated. Black arrows indicate the approximate orientations of the sightlines of some of the components. A blue arrow indicates the direction of the plasma current (I_p). Adapted from [21], with the permission of AIP Publishing.

discharges 49 447 and 49 452, the same total LFS fuelling rate (molecules s^{-1}) was used as in discharge 46 735, but it was distributed across two midplane LFS fuelling valves, the valves in sectors 9 and 11. The switch was programmed to occur at 0.50 s in discharge 49 447 and at 0.40 s in discharge 49 452. In these two discharges, the LFS fuelling was turned off 200 ms after being turned on, and the HFS fuelling was not turned back on. During the HFS-fuelling phases of all three discharges, a single midplane HFS fuelling valve was used, the valve in sector 2. To help the reader keep track of the analyzed discharges, above-mentioned similarities and differences in their fuelling are summarized in table 1. Turbomolecular pumps were used for gas exhaust. More details about the MAST-U gas system have been reported in a previous article [30].

Upon switching the fuelling side, immediate effects were observed consistently across the three discharges, as shown in figure 4, where the time axis has been normalized to the programmed fuelling switch time. More precise timings were inferred from a midplane D-alpha diagnostic whose sightline overlaps with the fuelling from the LFS valve in sector 9, which was used in all three discharges. As the fuelling gas interacts with the plasma edge, there is a huge increase in the D-alpha signal, as shown in figure 4(a). In each discharge, the LFS fuelling gas first reached the plasma 5 ms after the programmed fuelling switch time. A strong increase in the

Table 1. Details about the fuelling in the three discharges: the toroidal sectors (out of 12) in which the used HFS and LFS fuelling valves are located as well as the programmed fuelling switch times.

discharge	sector of HFS valve	sectors of LFS valves	switch time (s)
46 735	2	9	0.30
49 447	2	9, 11	0.50
49 452	2	9, 11	0.40

neutral pressure, starting approximately 10 ms after the switch time in discharge 49 452 and closer to 15 ms after the switch time in discharge 46 735, was measured by a fast ion gauge (FIG) [31] at the vacuum vessel wall, as shown in figure 4(b). Since the FIG is located at the end of a specialized tube, it reacts to pressure changes with a delay of a few milliseconds. Further delays may be explained by the time it takes for the fuelling gas to flow to the location of the FIG and create an increased pressure there. Assuming room temperature (0.025 eV), a deuterium molecule moves about 1000 m s^{-1}, thus traversing 1 m on a timescale of the order of 1 ms. In particular, the additional delay of a few milliseconds in discharge 46 735 may be because it is fuelled only from the valve in sector 9, which is about 3 m from the FIG in sector 12, while discharge 49 452 is also fuelled from the valve in sector 11, which is about 1 m from the FIG. These timings are approximative, since neither the delay in the FIG reaction nor the speed and dynamics of the fuelling molecules are known exactly. In addition to this transient asymmetry, the stronger increase in pressure in discharge 49 452, which is also explained by the differing distances from the valves to the FIG, is the first evidence of steady-state toroidal asymmetry in the neutral density distribution, which will be discussed in detail in section 3.2. An increase in the neutral pressure at the vessel wall is expected to translate to an increase in the neutral density in the SOL and plasma edge.

Four independent fast-ion diagnostics all measured decreases in signal when the fuelling side was switched, as shown in figure 4, panels (c)–(f), the exception being the FIDA system that views the plasma from sector 12. Since only the off-axis beam was used during the fuelling switch, both of the two FIDA views in MAST-U only saw a passive signal. The view from sector 12 overlaps with both of the midplane LFS fuelling valves that were used, as shown in figure 3. Like the standard D-alpha diagnostic (figure 4(a)), this FIDA view measured an immediate, huge increase in signal starting 5 ms after the programmed fuelling switch, as shown in figure 4(c). The corresponding channel in the FIDA view from sector 7, which is roughly on the opposite side of the plasma, shows an immediate, strong decrease in signal followed by a partial recovery over some tens of milliseconds. This is explained by how a FIDA signal is determined by both the fast-ion and neutral densities as well as by how the different processes involved occur on different timescales. The immediate decrease suggests an immediate and substantial decrease in beam-ion density near the plasma edge, i.e. an increase in beam-ion losses. The slower recovery is explained—similarly

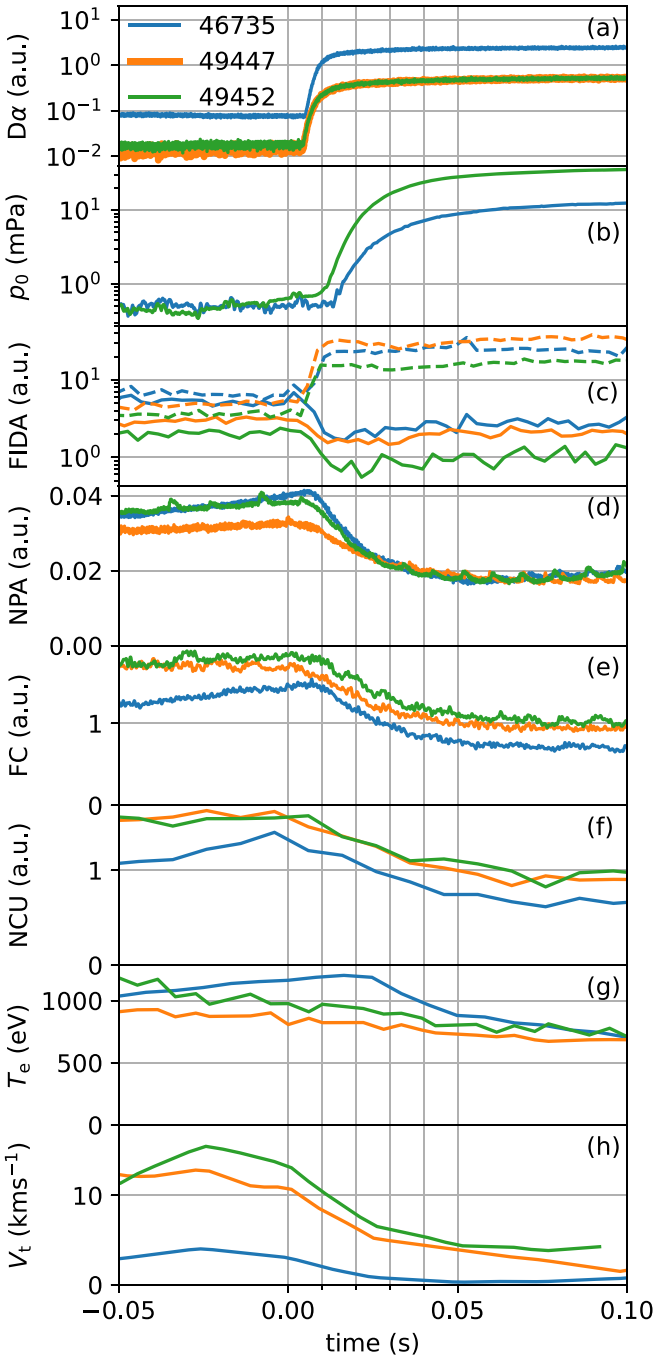

Figure 4. Time traces for the three discharges for the following quantities: midplane D-alpha (a.u.) (a), neutral pressure (mPa) at the vacuum vessel wall (b), FIDA (a.u.) (660.8 nm; channel 11 out of 11, which has the largest tangency radius, 1.43 (m) from views in sectors 7 (solid) and 12 (dashed) (c), SSNPA (a.u.) (channel 3 out of 16) (d), neutron rate (a.u.) from fission chamber (e), neutron rate (a.u.) from neutron camera (average of all channels) (f), core electron temperature (eV) (g) and plasma rotation as toroidal flow velocity (km s^{-1}) at major radius 1.32 m (h). Time abscissae are normalized to programmed fuelling switch time. No neutral-pressure data are plotted for discharge 49 447 because FIG was not operating.

to the timings in the FIG pressure measurements—by the time it takes for the fuelling gas to move around the vacuum vessel and cause an increase in the neutral density in the SOL region

seen by the FIDA view from sector 7. With regard to the production of FIDA light, when the neutral density does increase there, it partially compensates for the decrease in the beam-ion density. In addition to FIDA, signals measured by the SSNPA (figure 4(d)) as well as neutron emission rates measured by both the fission chamber (figure 4(e)) and neutron camera (figure 4(f)) decreased by about a factor of two within a few tens of milliseconds. Because the on-axis beam was not on during the fuelling switches, the SSNPA measured only passive fast-neutral fluxes from the interaction between beam ions and edge neutrals, as well as x-rays that the diagnostic unavoidably detects. The representative SSNPA channel 3 out of 16 (detects particles from a major radius = 1.38 m with a pitch $v_\parallel/v \approx$-0.33, where $v_\parallel$ is the velocity parallel to the magnetic field and v is the total speed) was chosen from the array that is filtered by a tungsten foil with a thickness of 100 nm (detects particles with energies $\gtrsim$15 keV). All of the decreases in fast-ion diagnostic signals suggest a substantial decrease in beam-ion density, which implies a substantial increase in beam-ion losses caused by the fuelling switch.

The central electron temperature, as measured by the core Thomson scattering system [32], decreased notably in discharge 46 735, as shown in figure 4(g). A decrease in temperature shortens the slowing-down time of fast ions, which decreases their density. Therefore, a temperature decrease may be expected to decrease emissions of FIDA light, neutral particles and neutrons, which can complicate the isolation of the impact of a certain loss mechanism. However, the temperature decrease is delayed by 20–30 ms, which is approximately the beam-ion slowing-down time. Hence, the temperature decrease is preceded by and cannot explain the immediate, strong decreases in the fast-ion diagnostic signals starting at 0.305 s. In fact, the decrease in temperature could be a result of beam-ion losses caused by the fuelling switch. Moreover, discharges 49 447 and 49 452 did not exhibit similar decreases in temperature following the fuelling switch; rather they exhibited slower temperature decreases spanning the full time range of interest. Nevertheless, the temperature decreases may have contributed to the total decreases in the fast-ion diagnostic signals, complicating the investigation of the impact of CX.

The plasma rotation was strongly slowed by the fuelling switch in all three discharges, as shown in figure 4(h). The toroidal flow velocity was calculated based on measurements by the UCLA Doppler back-scattering system [33] using the equation [34]

$$V_\mathrm{t} = \frac{\omega_\mathrm{d}}{k_\mathrm{p}} \frac{B}{B_\mathrm{p}}, \tag{1}$$

where ω_d is the Doppler shift, k_p is the poloidally directed scattered wave vector at cutoff, B is the total magnetic field strength and B_p the poloidal field strength at the point of scattering. Equation (1) implicitly assumes that the Doppler shift is dominated by $\boldsymbol{E} \times \boldsymbol{B}$ rotation (from the radial electric field $\boldsymbol{E}$) and that the turbulence velocity in the plasma rest frame is negligible. It also neglects poloidal rotation considerations, which should be small or at least subdominant [35]. The slowing of the rotation suggests an increase in beam-ion losses, because such losses would reduce the torque from the beam as well as give rise to a radial return current $\boldsymbol{j}_\mathrm{r}$, which causes a $\boldsymbol{j}_\mathrm{r} \times \boldsymbol{B}$ torque opposite to the rotation [36]. Another factor that may be slowing the rotation is drag caused by the interaction between the LFS fuelling gas and the LFS plasma edge. The slowing of the rotation could have further effects on the plasma. The decreased shear is expected to decrease energy confinement, resulting in temperature decrease and, by extension, decrease in the beam-ion density, which would be measured as a reduction in neutron emission. These compounding effects further complicate the investigation of the impact of CX.

The beam-ion CX process qualitatively explains the increase in beam-ion losses suggested by the measurements immediately after the fuelling switch. The beam energy was approximately 70 keV. The SOL and plasma edge typically feature neutral temperatures of the order of 1–100 eV and neutral densities of the order of 10^{15}–10^{17} m^{-3} [37–43]. Under such conditions, the CX mean free time is of the order of 100 μs–10 ms. Firstly, beam ions orbit the tokamak toroidally on timescales of 1–10 μs. Therefore, even those confined beam ions that make excursions into the SOL typically complete multiple toroidal orbits before undergoing CX. Secondly, the slowing-down time of the beam ions was estimated using ASCOT and TRANSP to be 20–40 ms. This is a characteristic timescale on which the fast-ion diagnostics are expected to react to changes in plasma parameters, such as density and temperature, due to their effects on the beam-ion density. Therefore, a toroidally localized influx of neutrals on the LFS, like those in discharges 46 735, 49 447 and 49 452, can result in CX losses on timescales much faster than many other processes, such as the slowing down of beam ions or the movement of fuelling gas around the vacuum vessel. These timescales explain, for example, the initial, immediate decrease in the FIDA signal, followed by a slower partial recovery. It should be noted that plasma parameters also affect the beam attenuation, implying that not only the number of CX losses but also the number of direct orbit losses of beam ions may change on timescales faster than the beam-ion slowing-down time.

While CX between beam ions and edge neutrals is mainly interpreted as a loss process, the fast CX neutral may also be launched inwards and reionized deeper inside the plasma. This inward transport depends on plasma conditions and can have significant effects, for example on the neutron emission, as has been reported for MAST-U and other devices [8, 10].

2.2. TRANSP modelling

For an improved understanding of what happened in the plasmas during the switch from HFS to LFS fuelling, TRANSP was used to interpretively model the three discharges. TRANSP is suitable for modelling such transient events since the code is designed for time-dependent simulation. Thomson scattering measurements of electron density and temperature were used. The ion temperature was assumed equal to the electron temperature, since the on-axis beam was

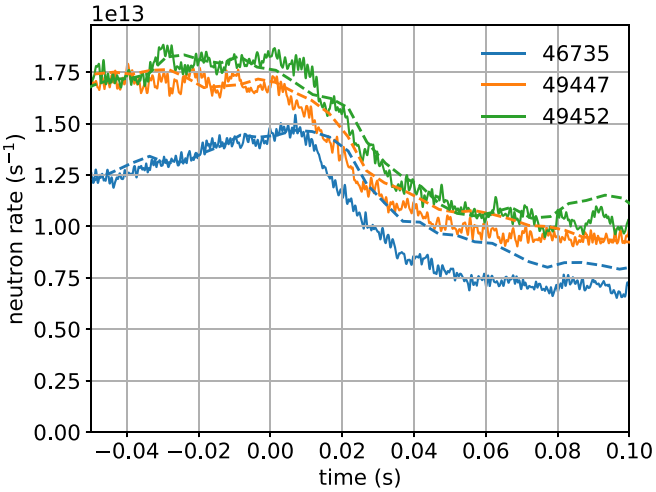

Figure 5. Total neutron emission measured by fission chamber (solid) and simulated by TRANSP (dashed) for the three discharges. TRANSP signal has been scaled to measurement based on average values from the 20 ms leading up to the programmed fuelling switch time (-0.02–0.00 s).

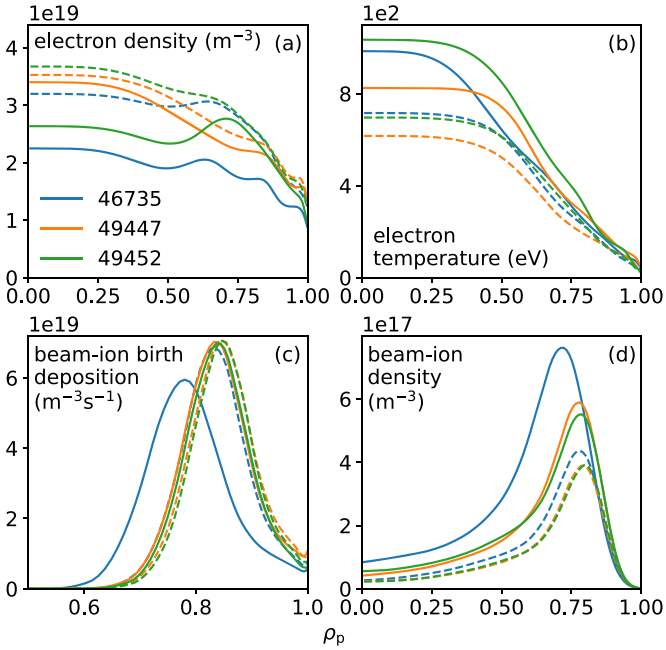

Figure 6. Collection of relevant measured ((a), (b)) and simulated ((c), (d)) radial profiles from TRANSP before (solid) and after (dashed) the fuelling switch for the three discharges. For discharge 46 735, data are shown for times 0.26 s and 0.38 s. For 49 447, 0.46 s and 0.58 s. For 49 452, 0.36 s and 0.48 s. Abscissa ρ_p is square root of normalized poloidal flux (see section 3.3).

not on during the fuelling switches and consequently there were no measurements of the ion temperature. When the on-axis beam was on for the last 200 ms of discharge 46 735, the ion temperature measured using charge-exchange recombination spectroscopy [44] was lower but within 50% of the electron temperature. In MU03 discharges with both beams, the ion temperature tended to be within 50% of the electron temperature. There was no attempt to replicate the impact of the fuelling switch on LFS SOL neutral density in TRANSP. The default, fixed SOL neutral density value for TRANSP simulations of MAST-U, $5 \cdot 10^{17}$ m^{-3}, was used throughout the discharges. The aim was to test if the direct measurements discussed in section 2.1 might be reproduced without directly accounting for the change in neutral density. TRANSP was run without anomalous fast-ion diffusion.

The total neutron emission estimated by TRANSP features similar relative drops as measured by the fission chamber, as shown in figure 5, but it is unclear if the underlying mechanisms are the same. Since absolute values of neutron emission simulated by TRANSP and measured by the fission chamber in MAST-U consistently disagree—the reason for which is still under investigation—and since this analysis is mainly concerned with relative changes in neutron emission, the TRANSP signal has been scaled to the measurement based on the average values from the 20 ms leading up to the programmed time of the fuelling switch. This does increase the uncertainty of the comparison, since the level of agreement in the neutron emission before the fuelling switch is unknown. Inspecting the figure further, there appear to be fluctuations and noise in both the measured and simulated signals, so it is difficult to make detailed comparison. However, at least in discharges 46 735 and 49 447, while TRANSP reproduces distinct drops in the neutron emission, the simulated, relative drops are slightly delayed and not quite as strong as the measured. This suggests that part of the change in the beam-ion distribution function is unaccounted for.

Changes in the plasma parameters explain the simulated drop in neutron emission in the time period following the fuelling switch. As shown in figure 6, the plasma density increases (figure 6(a)), which moves the beam-ion birth profile radially outwards (figure 6(c)). In terms of the radial birth rate, this effect appears minor in discharges 49 447 and 49 452, and more pronounced only in discharge 46 735. The simulated direct orbit losses increase from 10%–15% to 15%–20% in the three discharges. However, this increase in orbit losses is compensated by a decrease in CX losses from about 30% to about 25%. The sum of orbit and CX losses remains approximately unchanged at 40%–50%. The plasma temperature decreases (figure 6(b)). As a result, TRANSP calculates that the energy confinement time decreases by 20%–30% following the fuelling switch. This decrease in confinement time is stronger than what TRANSP estimates using the IPB98(y,2) scaling law [45], namely about 10%, suggesting transport that is not accounted for. The measured plasma profiles and simulated beam-ion losses change over tens of milliseconds, slower than the drop in the FIDA measurement from sector 7 (figure 4(c)). Both the increase in plasma density and decrease in plasma temperature shorten the beam-ion slowing-down time, which decreases the beam-ion density. Indeed, TRANSP estimates that the beam-ion density decreases substantially during the 80 ms following the fuelling switch, as shown in figure 6(d).

The TRANSP modelling further highlights the difficulty in ascertaining what exactly happens in the plasma following

the fuelling switch. The modelling shows that the changes in the plasma parameters during the transient stage can cause significant decrease in the beam-ion density. However, these changes occur on longer timescales than, for example, the measured drop in FIDA. It is unclear whether the changes in the measured plasma profiles are caused directly by the change in the fuelling or by increased losses of beam heating power, or a combination of both, or by something else. While further investigation could be performed using TRANSP by scanning over different values for the SOL neutral density, we had the capability to model the SOL neutral density more realistically. Moreover, bolometer measurements provided a unique opportunity to verify and quantify CX losses. Therefore, we employed the ASCOT code, which can use arbitrary inputs in the SOL and follow particle trajectories all the way to the wall, to directly model fast CX neutrals escaping the plasma, as is presented in section 3.

3. Quantifying CX losses using a bolometer

3.1. High bolometer power loads

Although bolometers are designed to detect electromagnetic radiation, energetic particles other than photons can contribute to bolometer signals [15]. During beam injection in MAST-U, the counter-beam channels of an array of resistive bolometers that view the midplane tangentially measure signals an order of magnitude higher than the co-beam channels, as has been reported for experiments of MU01 [15]. The co-beam signals are on the level expected from the electromagnetic radiation that the diagnostic is designed to measure.

The high bolometer signals, given that they appear during beam injection and only in channels directed counter to the beam injection, suggest bombardment by beam particles. Given the distance of the bolometer from the LFS separatrix, over 30 cm from the closest point on the aperture, charged particles cannot be expected to reach the bolometer. Fast CX neutrals can be expected to reach it. The counter-beam bolometer channels have the number designations 29–32 and tangency radii of 1.30, 1.10, 0.87 and 0.63 m, respectively.

In the MU02 and MU03 discharges analyzed in the present work, high signals were measured by channel 29, the outermost channel of the counter-beam bolometer, as shown in figure 7. This suggests that channel 29 was subject to substantial bombardment by fast CX neutrals, while channels 30–32, the rest of the counter-beam bolometer channels, were subject to only a little bombardment or none at all. The off-axis beam injected practically for the full durations of the discharges: 0.08–0.58 s in discharge 46 735 and 0.08–0.85 s in discharges 49 447 and 49 452. The measured bolometer signals have been heavily smoothed in time, so changes in a signal may have occurred faster in reality than is implied by the graph [15].

Two additional observations were made about the bolometer measurements shown in figure 7. In discharge 46 735, the on-axis beam was turned on at around 0.4 s, with similar power as the off-axis beam (figure 1), and the plasma disrupted at around 0.6 s. The increase of about 20% in the bolometer

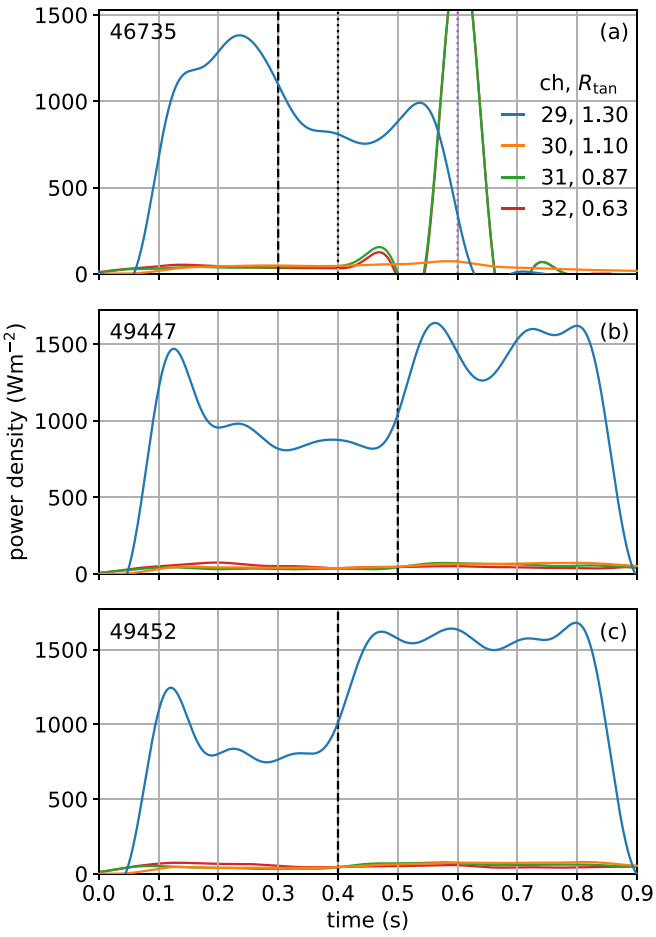

Figure 7. Measured power load densities on counter-beam bolometer channels as functions of time for the three discharges, in which the off-axis beam was on for the whole discharges. Channel ('ch') numbers and tangency radii R_{tan} (m) are given in the legend. Programmed time points for the switch from HFS to LFS fuelling are indicated by black dashed lines. Time points for when the on-axis beam was turned on and when the plasma disrupted in discharge 46 735 are indicated by black and purple dotted lines, respectively. Signals are heavily smoothed in time. The peaks and troughs in the signals of channels 31 and 32 in discharge 46 735 at around 0.6 s are ignored, since they are artefacts of the smoothing algorithm on the radiation spike in the plasma core when it disrupted.

signal of channel 29 during the on-axis beam injection before the disruption (figure 7) is approximately consistent with previously predicted CX losses of fast ions from the on-axis beam. Previous modelling of a MAST-U target scenario predicts 30% as many losses from the on-axis beam as from the off-axis beam, but the exact ratio is scenario-dependent [10]. CX losses are higher for the off-axis beam because it deposits ions closer to the edge on average. While the increase in the bolometer signal suggests CX losses for the on-axis beam in discharge 46 735, there are other possible explanations, e.g. the slow neutral-pressure increase that continues after 0.4 s according to the FIG. The result is uncertain also because the increase in the bolometer signal is delayed with respect to the on-axis beam. However, this delay may be explained by a competing

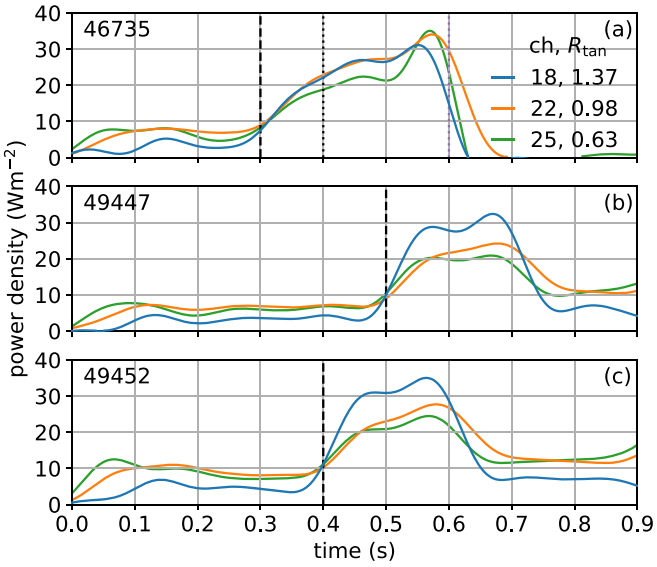

Figure 8. Measured power load densities on co-beam bolometer channels as functions of time for the three discharges. (See caption of figure 7 for details).

process causing signal decrease until around 0.45 s. Turning to the second additional observation, in discharges 49 447 and 49 452, the LFS fuelling was turned off 200 ms after being turned on, and the HFS fuelling was not turned back on, leaving the plasmas unfuelled for the remainder of their lifetimes. Yet, the higher bolometer signals, first caused by the switch to LFS fuelling, are maintained after fuelling is turned off. This suggests that the higher neutral density in the plasma region viewed by the counter-beam bolometer is maintained without continued LFS fuelling, likely due to recycling processes. Further investigation of CX losses of fast ions from the on-axis beam and of a lingering higher neutral density after fuelling has stopped is left to future work.

An estimate of the electromagnetic radiation emitted from the plasma is provided by the co-beam bolometer channels, which measured signals 1–2 orders of magnitude lower than the counter-beam bolometer channel 29 in the three analyzed discharges, as shown in figure 8. The lower signals on co-beam channels are explained by the anisotropic nature of the beam-ion-CX process. Since co-beam channels are evidently not hit by fast CX neutrals, they can be assumed to measure only the electromagnetic radiation emitted from the plasma. Further, since the plotted co-beam channels have similar tangency radii as the counter-beam channels and since the electromagnetic radiation is expected to be isotropic, the power loads measured by the co-beam channels provide estimates of the contribution by electromagnetic radiation to the power loads measured by the counter-beam channels [15]. Since this contribution is 1–2 orders of magnitude lower than the apparent contribution from fast CX neutrals in channel 29, it can be neglected in the following analysis.

It should be noted that the co-beam channels display signal increases when the fuelling is switched from the HFS to the LFS (figure 8). Unlike the signal increases that the fuelling switch causes in channel 29, which were discussed above, the co-beam signals decrease again once the fuelling is turned off. The co-beam bolometer is located in sector 12, and views the plasma in the counter-clockwise direction when viewing the tokamak from above. Thus, it overlaps with the LFS fuelling valves in sectors 9 and 11 (figure 3). It appears that the signal increases in the co-beam channels are directly tied to the LFS fuelling. Further investigation of this phenomenon is left to future work.

3.2. *Toroidal asymmetry*

It was qualitatively confirmed that the neutral density around the plasma is toroidally asymmetric during LFS fuelling. Figure 9 shows D-alpha radiation from the three discharges before and after the fuelling switch, as recorded by a high-speed-video (HSV) camera [46], which views the plasma from sector 8 (figure 3). The asymmetric brightness distributions after the switch show that LFS fuelling using the valves in sectors 9 and 11, or only the valve in sector 9, gives rise to a toroidally asymmetric neutral density around the plasma.

By considering the toroidal positions of the various elements in the experiments (figure 3) and the toroidal asymmetry they produce, certain features of the bolometer measurements shown in figure 7 can be qualitatively explained. In discharge 46 735, where only the LFS fuelling valve in sector 9 was used, the fuelling switch results in a decrease in the bolometer signal in channel 29. In discharges 49 447 and 49 452, where valves in sectors 9 and 11 were used, the switch results in an increase in the bolometer signal. The counter-beam bolometer channels, whose aperture is in sector 1, view a region spanning sectors 1–5, i.e. approximately the opposite side of the plasma torus from sector 9. The LFS neutral density probably increases everywhere around the plasma when switching to LFS fuelling valves (figure 9), but the beam power remains the same. Since the beam-ion population can be depleted, the toroidal asymmetry of the neutral density after switching to LFS fuelling can result in an increase in CX losses in some toroidal regions and in a decrease in others. A possible explanation for the bolometer measurements is then as follows. The valve in sector 11 causes enough of an increase in the neutral density at the bolometer sightlines compared to elsewhere around the plasma that the bolometer sees an increase in fast CX neutrals escaping in discharges 49 447 and 49 452. Conversely, when fuelling solely from sector 9 in discharge 46 735, the increase in neutral density at the bolometer sightlines is so low compared to around sector 9 that the beam-ion population is largely depleted by CX losses near sector 9, resulting in a decrease in CX losses at the bolometer sightlines. Indeed, as was mentioned in section 2.1, the pressure increase measured by the FIG in sector 12, i.e. between the fuelling valves and bolometer sightlines, is larger in discharge 49 452 than in discharge 46 735 despite equal total fuelling rates (figure 4(b)).

It was observed that the Thomson scattering measurements indicated significant electron density in the SOL during LFS fuelling in the three discharges: about 20% of core electron density extending about 5–10 cm outside the separatrix on the

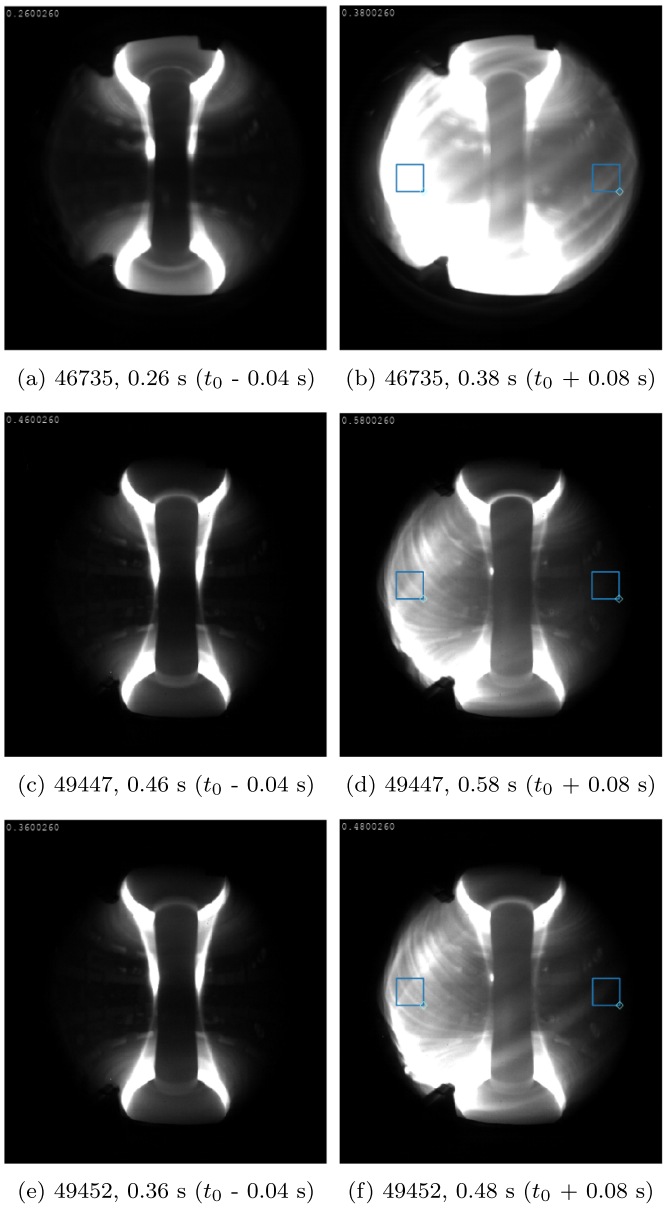

(a) 46735, 0.26 s (t_0 - 0.04 s) (b) 46735, 0.38 s (t_0 + 0.08 s)

(c) 49447, 0.46 s (t_0 - 0.04 s) (d) 49447, 0.58 s (t_0 + 0.08 s)

(e) 49452, 0.36 s (t_0 - 0.04 s) (f) 49452, 0.48 s (t_0 + 0.08 s)

Figure 9. D-alpha radiation during HFS fuelling ((a), (c), (e)) and during LFS fuelling ((b), (d), (f)) in the three discharges, as recorded by an HSV camera. Sectors 9 and 11, where the LFS fuelling valves reside, are to the left in these images. Discharge number and time point (and time point relative to fuelling switch time t_0) are given for each case. Blue squares indicate averaging areas used when estimating maximum and minimum brightnesses in section 3.5.

outer midplane. The Thomson scattering laser fires from sector 11 (figure 3). Given the strong fuelling from the nearby LFS valves in sectors 9 and 11, it is plausible that there is an ionization front protruding out of the separatrix at the measurement location. Since the magnetic field lines have an incline of about 30 degrees at the outer-midplane separatrix, such SOL plasma is lost to the divertors within about one-fourth of a toroidal revolution, making it a toroidally localized phenomenon. It is possible that the SOL plasma affects the attenuation of the off-axis beam, which injects counter-clockwise from sector 8 at 65 cm above the midplane. Since reconstructions of plasma profiles are only radially resolved and based on the Thomson scattering measurements in question, the inferred SOL plasma density was imposed everywhere around the plasma in modelling, which did have a limited influence on the simulation of the beam attenuation and the reconstruction of the neutral density in the present work. The indication of a significant and toroidally localized plasma density in the MAST-U SOL during LFS fuelling gives reason to review the reconstruction of plasma profiles. However, this ambitious task goes beyond the scope of this study.

3.3. Simulating bolometer power loads using ASCOT

Since charged particles cannot be expected to reach the bolometer, the high power loads measured on the bolometer provide a unique opportunity to investigate CX losses, isolated from other loss mechanisms. A scheme was devised to simulate the phenomenon using ASCOT to verify the reason for the high bolometer signals as well as to quantify the suspected CX losses. ASCOT is a Monte Carlo code that follows the orbits of a minority population of particles in a detailed reconstruction of a steady-state plasma in an unlimited, 3D computational domain, and estimates the full 6D phase-space distribution function of the population. ASCOT is suitable for modelling particles escaping the plasma and hitting a component in the device wall, since the code can follow particles through a realistic SOL and all the way to an arbitrarily detailed 3D representation of the wall.

The target surfaces of the bolometer diagnostic are rectangular foils that are 1.3 mm wide and 3.8 mm high. These foils correspond to the channels (figure 7) of the diagnostic. There are four foils inside an aperture with an opening tangentially towards the plasma. The geometry and other technical details of the MAST-U bolometer system have been reported previously, complete with illustrations [15]. Radiation and particles emitted from the plasma must travel through the opening in the aperture to reach a foil. The high bolometer signals were observed only in channels directed counter to the beam injection, i.e. clockwise when viewing the tokamak from above. This is expected from the beam-ion CX effect, which is anisotropic, unlike the electromagnetic radiation that the bolometer is designed to measure. The co-beam bolometer channels were omitted from the simulations for this study.

A CAD (Computer-Aided Design) model of the counter-beam bolometer diagnostic was included in a virtual 3D reconstruction of the MAST-U wall [10]. Since the bolometer foils are small targets for the markers (virtual particles) in an ASCOT simulation of the entire tokamak, statistics was a challenge. To improve statistics, copies of the bolometer model were placed all around the tokamak by varying the toroidal angle of the position. Toroidal symmetry was assumed at this stage, although the assumption is false during LFS fuelling, as was discussed in section 3.2. Toroidal asymmetry is simulated in section 3.5. A total of 360 bolometer copies were used, with uniform toroidal spacing, effectively increasing the target area by a factor of 360. Figure 10 shows a part of the ring of virtual bolometer copies, both from the front (figure 10(a)) and from above (figure 10(b)). In figure 10(a), the foil corresponding to channel 29 can be seen through the openings in the apertures,

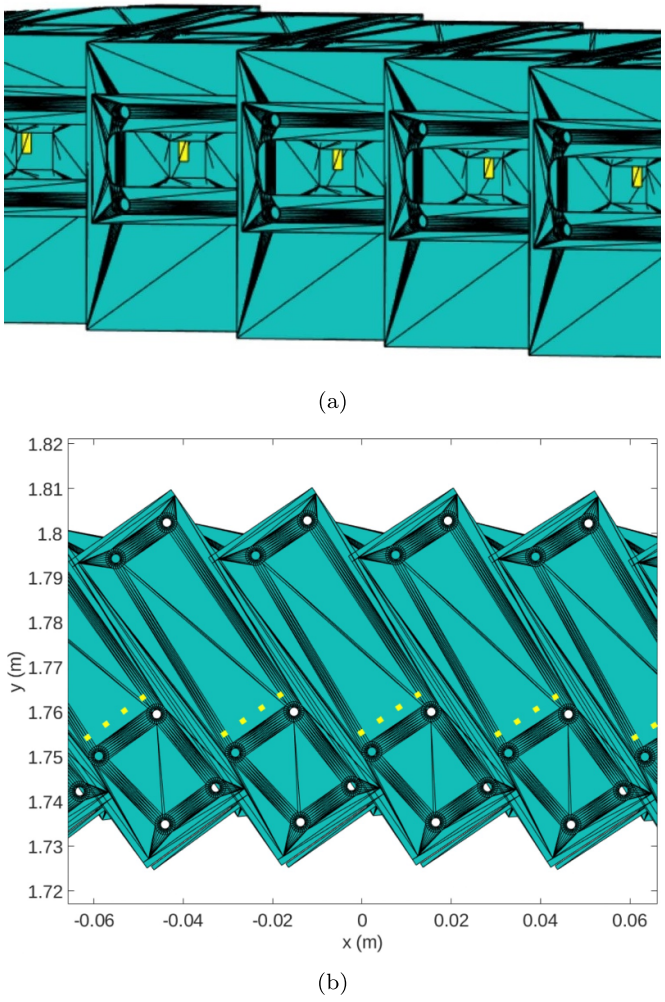

Figure 10. Part of the ring of 360 copies of the counter-beam bolometer model that was used in ASCOT simulations, as viewed from the front (a) and above (b). In (a), the foil (yellow) corresponding to channel 29 can be seen through the openings in the apertures. In (b), the axes display standard machine coordinates, and the positions of all four foils (yellow) in the *x*-*y* plane are indicated (would in reality be obscured by aperture roof).

and, in figure 10(b), the positions of all four foils in the *x*-*y* plane are indicated. Despite tightly packed bolometer copies, apertures did not obscure any sightlines through the openings of neighbouring apertures to their corresponding foils. Given the distance of the bolometer from the plasma, charged particles following curved trajectories to the foils were not expected. Irrelevant support structures of the aperture model were omitted to avoid unnecessary overlapping structures in the final wall model.

ASCOT, with its model for fast-ion CX reactions [10, 13], was used to simulate populations of beam ions under the effect of CX reactions to model fast CX neutrals hitting the counter-beam bolometer foils. For each of the three discharges, 46 735, 49 447 and 49 452, simulations were performed 40 ms before and 80 ms after the programmed time of the fuelling switch, when the plasma density and temperature as well as the magnetic equilibrium were in relatively steady states. To generate the beam-ion populations for the ASCOT simulations, 20 million markers were simulated for each case using the BBNBI code [47] (version corresponding to ASCOT5) from the ASCOT suite of codes that models the attenuation of a neutral beam in a plasma. The beam-ion populations were represented by a little fewer than 20 million markers, because those that ended up as shine-through were omitted. In the six cases simulated, the shine-through was 9%–16% of the injected beam power. As discussed in section 3.2, during LFS fuelling, the possibly overestimated plasma density in the SOL caused unusually high beam attenuation in the SOL.

The density and temperature of background neutrals, key in CX modelling, were reconstructed on the outer midplane using the 1D kinetic neutral transport code KN1D [48, 49], which takes as input the electron density and electron and ion temperatures as well as the neutral pressure at the vessel wall. As in the TRANSP modelling in section 2.2, Thomson scattering measurements of electron density and temperature were used, and the ion temperature was assumed equal to the electron temperature. The fast-particle CX and reionization reactions are insensitive to temperature [10]. As discussed in section 3.2, during LFS fuelling, the significant electron density measured in the SOL affected the neutral density reconstruction. The plasma density and temperature profiles were smoothed using a profile-fitting code that fits basis-function splines to the measured data [50]. The neutral pressure at the wall was measured using a midplane FIG. Since the FIG was not operating in discharge 49 447, the measurement of the similar discharge 49 452 was used as a proxy, shifted by 100 ms like the programmed fuelling switch time. These two discharges were programmed to be exactly the same, with the exception of the 100 ms shift in the timing of the fuelling switch. The claim of similarity is further supported by the overlapping D-alpha measurements shown in figure 4(a). Since ASCOT cannot yet model CX with molecules, the atomic and molecular densities estimated by KN1D were summed and approximated as a purely atomic neutral background. This is a good approximation when modelling beam-ion CX, as has been argued previously [13]. Briefly, under MAST-U conditions, a fast ion has a 0%–50% higher probability for CX with a molecule than with an atom [51]. The temperature for the combined neutral density was calculated as the density-weighted average of the atomic and molecular temperatures estimated by KN1D. Beam-halo neutrals were omitted from the modelling, since only the off-axis beam was used, meaning the beam halo formed around 65 cm above the midplane. CX neutrals travelling through the opening in the bolometer aperture and hitting the foils would have to be born on the midplane. Furthermore, since the beam-halo neutral density is low compared to the density of neutrals coming in from outside the plasma, this omission is not expected to have a significant impact on the total CX losses. At this stage, the neutral density and temperature in the plasma and SOL were assumed to be poloidally and toroidally symmetric (constant in the poloidal and toroidal angles) and were defined as 1D functions of the flux coordinate $\rho_\mathrm{p} = \sqrt{(\psi_\mathrm{p} - \psi_\mathrm{p,ax})/(\psi_\mathrm{p,sep} - \psi_\mathrm{p,ax})}$, where ψ_p is the poloidal flux, and $\psi_\mathrm{p,ax}$ and $\psi_\mathrm{p,sep}$ are its values at the magnetic axis

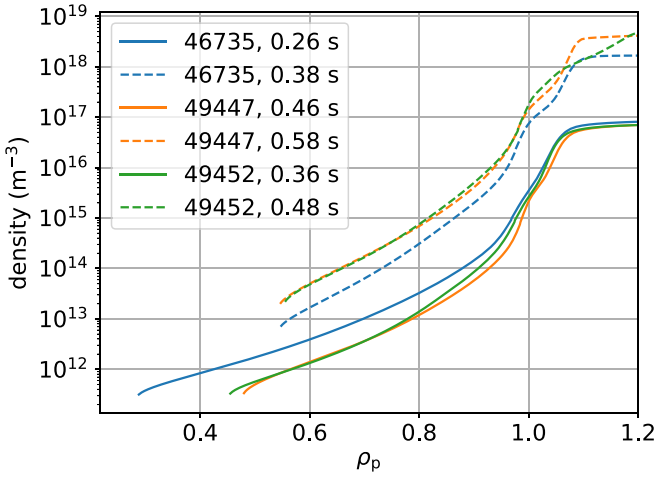

Figure 11. Outer-midplane neutral deuterium density reconstructions for the three discharges as functions of the flux coordinate ρ_p (separatrix at 1.0), based on KN1D modelling. In the plasma core, where KN1D gave no results and density is expected negligible, density was set to zero.

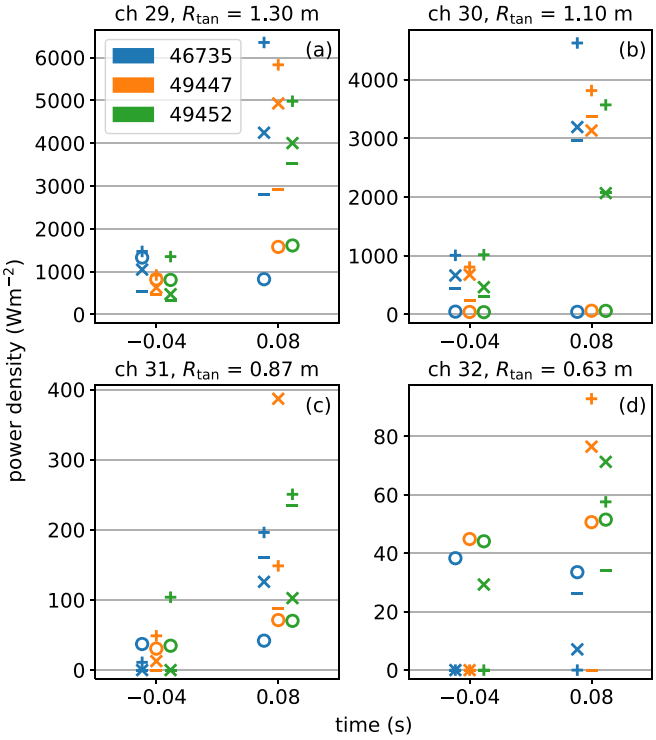

Figure 12. Measured (○) and simulated power load densities on the four counter-beam bolometer channels during HFS (−0.04 s) and LFS (0.08 s) fuelling in the three discharges. Results simulated using the measured (×), halved (-) and doubled (+) neutral pressure are included. Channel ('ch') number and tangency radius R_{tan} are given above each panel. Time abscissae are normalized to the programmed fuelling switch time. Data points for discharges 46 735 and 49 452 are slightly shifted along the time axis for readability.

and at the separatrix, respectively. The poloidal flux was calculated using the EFIT++ code [52, 53] based on magnetic measurements. The neutral density and temperature functions calculated by KN1D were mapped from the major radius to ρ_p on the outer midplane, where the Thomson scattering and FIG measurements were taken. The assumption of a poloidally symmetric neutral density based on an outer-midplane reconstruction is considered a good approximation for analysis of beam ions in MAST-U, as has been argued previously [10, 13]. Briefly, beam-ion orbits are weighted towards the outer midplane in the spherical geometry, with practically none reaching near the edge on the HFS or in the top or bottom of the plasma. A poloidally realistic neutral density would typically be higher closer to the divertors due to higher recycling, which would be expected to increase CX losses from regions closer to the divertors.

Figure 11 shows the reconstructed neutral density profiles in the confined plasma and in the part of the SOL that is reachable by beam ions. In accordance with the rise in neutral pressure (figure 4(b)), the neutral density is 1–2 orders of magnitude higher during LFS fuelling than during HFS fuelling in the three discharges. Based on these reconstructions, the SOL neutral density assumed in the TRANSP modelling in section 2.2 ($5 \cdot 10^{17}$ m^{-3}) is greatly overestimated during HFS fuelling, especially since the simulated neutral density in TRANSP increases to its SOL value immediately outside the separatrix.

It should be noted that reconstructed neutral densities for HFS-fuelled plasmas were significantly higher in a previous article on similar work [13]. The reason is that, after the analysis for the previous article had been performed, the FIG calibration was updated such that the pre-discharge value is subtracted from the signal measured during a discharge. As a result, neutral pressure measurements give lower values now.

3.4. *Toroidally symmetric results*

Out of the nearly 20 million markers used in each ASCOT simulation case, a total of the order of tens or hundreds of markers hit the counter-beam bolometer foils. This is enough to get estimates of the power loads on the foils.

Figure 12 shows the measured and simulated power loads on the counter-beam channels of the bolometer during HFS fuelling and during LFS fuelling for the three discharges that were studied. Because of the low statistics of markers hitting bolometer foils in the simulations, noise of the order of some tens of percent should be expected in the simulated power loads on channels 29 and 30, which have tens of hits during HFS fuelling and around a hundred hits during LFS fuelling. On channels 31 and 32, since they tend to have only a few hits, the noise is of the same order as the signal, which explains why a higher neutral density resulted in a lower power load in some cases. Nevertheless, if all three discharges are considered simultaneously to mitigate the noise issue, the results are sufficient to estimate the order of magnitude of the power loads on channels 31 and 32.

The power loads measured on the counter-beam bolometer foils during HFS fuelling were approximately reproduced in simulations in all three discharges, with the exception of channel 30, as is shown in figure 12. In each discharge, the

simulated power load on channel 29 agrees with measurement during HFS fuelling to within 40%, as shown in figure 12(a). Similar power loads were simulated on channel 30 as on channel 29, which overestimates the measurements by an order of magnitude during HFS fuelling (figure 12(b)). However, as this is a middle channel, the overestimation could be caused by a small spatial inaccuracy in the simulation inputs. The low loads on channels 31 and 32 (figures 12(c) and (d)), if all three discharges are considered simultaneously to mitigate the noise issue, were reproduced during HFS fuelling in the sense that they are an order of magnitude lower than the loads on channel 29. It should be kept in mind that, unlike the simulated power loads, the measured loads also include radiation, which is expected to be on a similar level for the counter-beam channels as the loads measured for co-beam channels (figure 8), as explained in section 3.1. Loads on channels 29 and 30 were overestimated during LFS fuelling. Because of the high statistical noise, it is difficult to interpret the simulated loads on channels 31 and 32 also during LFS fuelling, but there appears to be similar relative overestimation for channel 31 as for channel 29 and no overestimation for channel 32.

The successful reproduction of the power loads on channels 29, 31 and 32 during HFS fuelling shows that the beam-ion CX process does, indeed, explain the high bolometer measurements. Further, it indicates that the neutral density and other simulation inputs are realistic during HFS fuelling, at least in those plasma regions from which CX neutrals can bombard the bolometer foils. Therefore, the simulations can be expected to provide realistic estimates of the overall impact of CX on the beam-ion population. It is estimated that 9%, 7% and 7% of the beam power that is originally deposited in the plasma is lost due to CX during HFS fuelling in discharges 46 735, 49 447 and 49 452, respectively. Power lost due to CX is here approximated as the power contained in markers that hit the wall as neutrals, which has been deemed a good approximation [13].

It is recognized that accurately reconstructing the neutral background is difficult, whether it be due to inaccuracy in the neutral pressure measurements, inaccuracy in the reconstruction of the plasma density and temperature profiles, or something else. Therefore, the neutral background was not assumed accurate, but a sensitivity scan was performed. The measured neutral pressure was halved and doubled, and the simulations were rerun with the resulting lower- and higher-density neutral backgrounds. The resulting, alternative simulated bolometer power loads are included in figure 12. All of the precise simulation results as well as additional details and discussion are gathered in the appendix.

The measured bolometer signal for channel 29 during HFS fuelling consistently falls between the results simulated for the actual, measured neutral pressure and the double pressure (figure 12(a)). This suggests that the neutral density is underestimated by about a factor of 1.5 when calculated based on the measured neutral pressure, possibly due to remaining uncertainty in the FIG calibration, or that the CX rate is underestimated because molecules are approximated as atoms. The simulated losses of beam power for all three neutral pressures for all six plasma cases are gathered in table 2. Based on the above reasoning, the true value for the loss of beam power due to CX during HFS fuelling is between the estimates from the case with the measured neutral pressure and the case with double pressure, i.e. 9%–14%, 7%–12% and 7%–13% in discharges 46 735, 49 447 and 49 452, respectively. The relatively small increase in CX losses during LFS fuelling when doubling the neutral pressure is explained by depletion of the beam-ion population near the plasma edge.

Table 2. Simulated loss of beam power (excluding shine-through) due to CX (hit the wall as a neutral) in each case. Cases are specified by discharge number, time point (s) and whether the measured neutral pressure ('$\times p_0$' = '1') was used when reconstructing the neutral background or half ('0.5') or double ('2') the measured pressure.

			power loss	
discharge	time	$\times p_0$	MW	%
46 735	0.26	0.5	0.07	5
		1	0.12	9
		2	0.19	14
	0.38	0.5	0.38	26
		1	0.53	37
		2	0.69	47
49 447	0.46	0.5	0.06	4
		1	0.11	7
		2	0.19	12
	0.58	0.5	0.67	43
		1	0.86	54
		2	1.03	65
49 452	0.36	0.5	0.06	4
		1	0.11	7
		2	0.19	13
	0.48	0.5	0.55	36
		1	0.72	47
		2	0.89	58

The overestimation of the power loads on channel 30 and, during LFS fuelling, on channel 29 indicate inaccuracies in the simulation inputs. The neutral density, which is notoriously difficult to reconstruct, is the obvious first candidate. Uncertainty in the Thomson scattering measurements, particularly in the SOL and near the separatrix, upon which not only the neutral density reconstruction but also the simulated beam attenuation depends sensitively, makes the beam-ion birth distribution another likely candidate. Moreover, as was discussed in section 3.2, the plasma density in the SOL may have been overestimated during LFS fuelling, causing false ionization of beam particles in the SOL. An overestimated neutral density would explain more marker hits on all channels. It is suspected that the neutral density during LFS fuelling was overestimated in the simulations reported on in this section, especially in the region viewed by the counter-beam bolometer, as will be discussed below. The overestimation of the load on channel 30 during HFS fuelling could also be caused by a mismatch in the absolute positioning of the physical and virtual bolometers.

In this section, the ASCOT modelling did not account for toroidal asymmetry in the neutral density, which may explain

why the power loads on the bolometer were overestimated during LFS fuelling. This hypothesis is supported by how the discrepancy between measured and simulated bolometer loads (figure 12) is greater in discharge 46 735, which only used the LFS fuelling valve in sector 9, than in discharges 49 447 and 49 452, which also used the valve in sector 11, which is closer to the region viewed by the bolometer (figure 3). The ASCOT neutral density input assumed a global increase in line with the pressure measurement in the one operating main-chamber FIG, which is in sector 12. In the case of discharges 49 447 and 49 452, since one of the LFS fuelling valves used is in sector 11, close to the FIG, a neutral density estimate based on a measurement by the FIG not only fails to reproduce the toroidal asymmetry but also is likely an overestimation of the average neutral density around the plasma. Hence, the simulations for time periods during LFS fuelling in these two discharges were not only incapable of accounting for the toroidal asymmetry but also likely overestimated the total CX losses. Accurately simulating fast CX neutrals hitting the bolometer during LFS fuelling would require a reconstruction of the toroidally asymmetric neutral density. While accurately modelling the toroidal asymmetry goes beyond the scope of this article, a first study on the impact of a toroidally asymmetric neutral density distribution was performed and is reported in section 3.5.

3.5. *Toroidally asymmetric results*

To test the hypothesis that the overestimation of bolometer loads during LFS fuelling in section 3.4 is due to toroidal asymmetry, proof-of-principle-level toroidally asymmetric modelling was performed. The cases with LFS fuelling, i.e. discharge 46 735 at 0.38 s, discharge 49 447 at 0.58 s and discharge 49 452 at 0.48 s, were simulated using ASCOT with simple toroidally asymmetric neutral density distributions. Realistically reconstructing the toroidal asymmetry in the neutral density is a challenging undertaking and is left to future work.

The 1D neutral background data described in section 3.3 was mapped to a 3D grid, and the density was made asymmetric in the toroidal angle based on a simple, empirical model. The neutral density distribution was assumed to have its maximum at the toroidal location of the fuelling epicentre and its minimum at the opposite side of the plasma torus, and the density function was assumed linear in the toroidal angle. In discharge 46 735, the fuelling epicentre was the location of the one fuelling valve that was used, the valve in sector 9 (figure 3). In discharges 49 447 and 49 452, the epicentre was the midpoint between the two valves that were used, the valves in sectors 9 and 11. Toroidal locations of components were approximated as the midpoints of the sectors where they reside. For each case, the absolute value of the neutral density was determined based on the corresponding 1D neutral density profile such that the density of the 3D neutral background matched the density of the 1D neutral background at the toroidal location of the FIG (sector 12). The 1D neutral background based on the measured neutral pressure was used. The sensitivity scan was not repeated, since the focus here is on the impact of the toroidal asymmetry of the neutral density distribution. The neutral temperature was left symmetric in the toroidal angle.

The D-alpha brightness data from the HSV camera (figure 9) was used to estimate the ratio between the maximum and minimum neutral density values along the toroidal angle during LFS fuelling. If it is assumed that metastable states due to electron excitation dominate over metastable states due to recombination and charge-exchange reactions, the latter two can be neglected and the D-alpha emissivity can be calculated as [54]

$$\epsilon_{3\to2} = \mathrm{PEC}^{(\mathrm{exc})}_{3\to2} n_\mathrm{e} n^0_\mathrm{D}, \tag{2}$$

where $\mathrm{PEC}^{(\mathrm{exc})}_{3\to2}$ is the excitation photon emissivity coefficient (depends on electron density and temperature) for the transition from the energy state $n = 3$ to $n = 2$ (n is the principal quantum number), n_e is the electron density and n^0_D is the neutral-deuterium density. Based on equation (2), the brightness is proportional to the neutral density when the electron density and temperature remain fixed. The electron density and temperature were assumed toroidally symmetric, and the ratio between the maximum and minimum neutral density values was estimated as the ratio between the maximum and minimum brightnesses. This assumption is a source of uncertainty, since there may be toroidally localized electron density in the SOL near the LFS fuelling valves, as discussed in section 3.2. The maximum and minimum brightnesses were estimated as the average brightnesses inside small squares on the left and right sides, respectively, of the HSV image. The squares are indicated in figures 9(b), (d) and (f). The ratios evaluated for discharges 46 735, 49 447 and 49 452, during LFS fuelling, are approximately 3.4, 13 and 13, respectively.

The lower brightness ratio in discharge 46 735 may be explained by the toroidal point of minimum brightness being further behind the plasma on the right side of the image (figure 9(b)) than for discharges 49 447 and 49 452 (figures 9(d) and (f)). The HSV camera views the plasma from sector 8, so it makes for a substantial difference whether the full fuelling rate comes from the adjacent sector 9 or that same fuelling rate is evenly distributed between sectors 9 and 11. Another reason that the brightness ratio for discharge 46 735 may be underestimated is that figure 9(b) appears to be saturated on the left side. For these reasons, the ratio 3.4 should be considered a conservative estimate of the brightness variation in discharge 46 735.

Adequate statistics for toroidally resolved marker hits on bolometer foils were not possible. Instead, the toroidally resolved deposition of CX neutrals on the whole wall was the quantity of interest in this modelling of the toroidal asymmetry. To save on computational resources, fewer markers were used for these simulations than in section 3.3. BBNBI was run with 2 million markers to generate beam-ion populations for each of these ASCOT simulations.

The toroidally asymmetric neutral density distribution gave rise to a toroidally asymmetric power deposition on the wall from CX losses, again approximated as the power contained

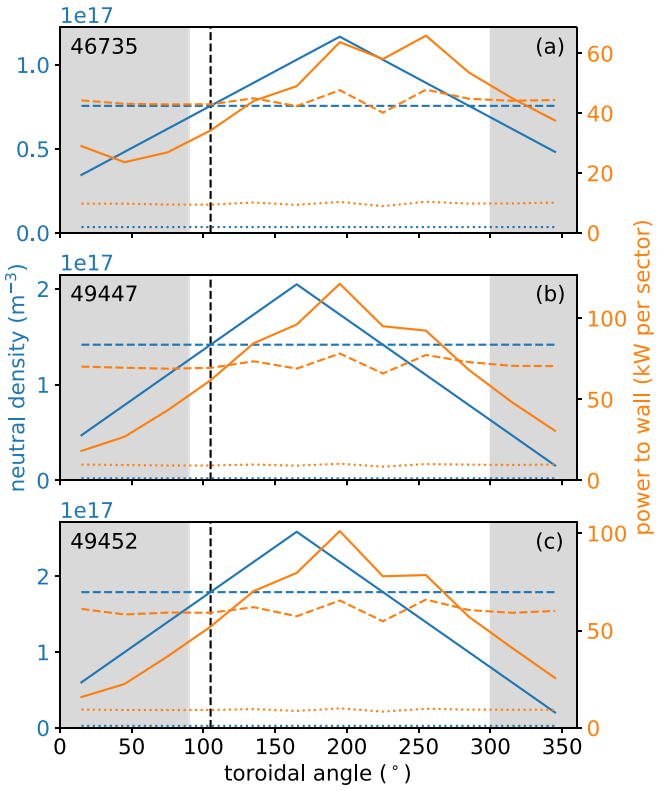

Figure 13. Neutral density at the separatrix (blue) and power deposition from fast CX neutrals to the wall (orange) in the three discharges, during LFS fuelling, simulated both using toroidally asymmetric (solid) and toroidally symmetric (dashed) neutral density distributions, as well as during HFS fuelling (dotted). Sectors viewed by the counter-beam bolometer are indicated by grey shading. Location of FIG is indicated by black vertical dashed line. Toroidal coordinate runs counter-clockwise, starting between sectors 3 and 4 (figure 3).

in markers that hit the wall as neutrals. Figure 13 shows the toroidally resolved neutral density at the separatrix and power deposition from fast CX neutrals to the wall during LFS fuelling. The data resulting from the use of toroidally symmetric neutral density distributions during LFS fuelling as well as the data for the cases during HFS fuelling (toroidally symmetric) are also shown for comparison. In the toroidally asymmetric cases, the maximum power deposition is shifted from the maximum neutral density in the positive toroidal direction, which is explained by how the beam injects tangentially in the positive toroidal direction. The modest fluctuations in the power-deposition graphs compared to the neutral-density graphs are likely due to protruding components in the 3D wall.

The results in figure 13 verify the hypothesis that the overestimation of bolometer power loads during LFS fuelling in section 3.4 is explained by toroidal asymmetry. In discharges 49 447 and 49 452, in the region viewed by the bolometer, i.e. sectors 1–5 (shaded in figure 13), the power loads resulting from the toroidally asymmetric neutral density are 1–4 times lower than the loads resulting from the toroidally symmetric neutral density. In section 3.4, the bolometer loads on channel 29 in discharges 49 447 and 49 452 were overestimated by a factor of 2–3 (2–4 when including sensitivity scan) during LFS fuelling. In discharge 46 735, since the power deposition simulated during LFS fuelling with the toroidally asymmetric neutral density is not lower than the power deposition simulated during HFS fuelling at any toroidal angle, the measured decrease in the power load on channel 29 (figure 7(a)) is not demonstrated. However, this could be due to underestimation of the full toroidal variation of the neutral density because of the HSV camera having a poor vantage point for this discharge, as discussed above. Moreover, as discussed above, this modelling of the toroidal asymmetry features several approximations and simplifications, so precise results cannot be expected. The results of this section amount to a proof of principle, explaining the overestimation of the bolometer loads during LFS fuelling, as simulated using toroidally symmetric neutral density distributions in section 3.4.

While precise analysis of beam-ion CX during LFS fuelling is not yet possible, the results suggest significantly higher CX losses during LFS fuelling than during HFS fuelling. As expected based on the discussion in section 3.4 about the proximity of the fuelling to the FIG, the total CX losses in discharges 49 447 and 49 452 were lower using the toroidally asymmetric neutral density distribution, but only slightly lower. Switching from the symmetric to the asymmetric neutral density in the 2 million-marker simulations, the losses reduced from 56% to 51% for discharge 49 447 and from 47% to 43% for discharge 49 452. Similarly as when doubling the neutral pressure during LFS fuelling in section 3.4, the relatively small difference is explained by depletion of the beam-ion population near the plasma edge. In discharge 46 735, the total losses remained the same, 35%. This is explained by the FIG being exactly midway between the neutral-density maximum at the LFS fuelling valve in sector 9 and the minimum on the opposite side of the torus in sector 3, since it means that the 1D neutral density is the average of the 3D neutral density along the toroidal angle. The results of section 3.4 and the present section suggest that 40%–60% of the beam power that is originally deposited in the plasma is lost due to CX during LFS fuelling in the analyzed discharges. The increase in the loss of heating power caused by the fuelling switch is roughly consistent with the decrease in energy confinement time calculated by TRANSP in section 2.2, keeping in mind that the SOL neutral density was overestimated in the TRANSP simulations during HFS fuelling and kept constant through the fuelling switch. Given that the LFS fuelling used in the analyzed discharges was stronger by about a factor of two than what is typically used in MAST-U (section 2.1), the total CX losses simulated in the toroidally symmetric 20 million-marker ASCOT simulations with half the measured neutral pressure (table 2) provide a rough estimate of typical CX losses of off-axis beam power during LFS fuelling: 30%–40%.

4. Summary

In response to early results that indicated significant CX losses of beam ions, dedicated experiments were performed in

MAST-U to study the phenomenon. In three similar L-mode discharges, featuring only the off-axis neutral beam (during times of primary interest), the fuelling was switched from HFS to LFS valves to increase the neutral density in the LFS SOL and plasma edge. Direct measurements showed a strong increase in background neutral pressure and indicated a strong decrease in beam-ion density. While the CX process qualitatively explains the observations, TRANSP modelling demonstrated that measured changes in the plasma parameters can cause significant decrease in the beam-ion density, highlighting the difficulty in isolating the role of CX. Bolometer measurements presented a unique opportunity that was exploited to verify and quantify CX losses.

The MAST-U bolometer had measured an order of magnitude higher signals than usual during neutral beam injection, although only in the injection direction, indicating particle bombardment. Since charged particles should be unable to reach the bolometer, fast CX neutrals originating from the population of beam ions were suspected. To investigate this hypothesis, the fast-ion orbit-following code ASCOT was used to simulate the population of beam ions in the presence of CX reactions with a model of the bolometer embedded in the virtual 3D wall. The measured power loads on the bolometer were partially reproduced during HFS fuelling, verifying CX losses of approximately 10% of the off-axis beam power (excluding shine-through). Bolometer power loads were overestimated during LFS fuelling, which was suspected to be caused by toroidal asymmetry in the neutral density distribution that could not be accounted for in the initial modelling. Additional modelling was performed using a simple toroidally asymmetric neutral density distribution. The results demonstrate that toroidal asymmetry explains the overestimated bolometer loads. The results further suggest losses of up to approximately 50% of the off-axis beam power during LFS fuelling, keeping in mind that particularly strong LFS fuelling was used in the analyzed discharges. Precise analysis of LFS-fuelled plasmas is left to future work when the toroidal asymmetry can be accurately modelled or toroidally symmetric LFS fuelling is available. While this study did not include modelling of fast ions from the on-axis beam, a possible experimental indication of CX losses also from the on-axis beam was noted.

The estimated loss of power due to CX during HFS fuelling, approximately 10%, is comparable to estimates of power imbalance in MAST-U and JET, over 25% [16, 17], suggesting that CX losses may explain part of the observed power deficit. MAST-U is being upgraded with a cryoplant, which is expected to reduce the background neutral density. The ability demonstrated here to quantify CX power losses not only enables more accurate power balance calculations but also provides a method for gauging the effectiveness of the cryoplant at improving the plasma performance. The comparison of ASCOT simulations and bolometer measurements could possibly be made more efficient in the future, for example by developing a scheme for interpolating a distribution of lost particles at an arbitrary target. The evidence provided for increased CX losses during LFS fuelling will help design successful experiments with LFS fuelling. While MAST-U will have more LFS fuelling valves operating in the future, which will reduce the toroidal asymmetry noted in this study, improvements in the reconstruction of the neutral density distribution are envisioned. Such improvements include descriptions of the poloidal and toroidal asymmetries due to recycling from the divertors and the positions of fuelling valves. This will allow quantification of CX losses during LFS fuelling, which will enable more accurate modelling of the impact of CX on beam ions. On a more general note, switching from HFS to LFS fuelling was found to have profound effects on the MAST-U plasma, e.g. strongly slowing the rotation, which warrants further study towards an improved understanding of LFS-fuelled plasmas. Further TRANSP modelling would be useful, a natural next step being the use of measured or TRANSP-predicted ion temperatures.

Data availability statement

The data that support the findings of this study are openly available at the following URL/DOI: https://doi.org/10.14468/h59b-p097 [55].

Acknowledgment

We thank Rory Scannell for help with the FIG, Edward Parr for help with the SSNPA, Marco Cecconello for help with the neutron camera, Bhavin Patel for help with TRANSP, Chris Bowman for help with the profile-fitting code, Roy McAdams for help with the neutral beam, and Konsta Särkimäki for help with ASCOT. The ASCOT simulations were carried out on the EUROfusion High Performance Computer, Marconi-Fusion, at CINECA. We acknowledge the computational resources provided by the Aalto Science-IT project. This work has been carried out within the framework of the EUROfusion Consortium, funded by the European Union via the Euratom Research and Training Programme (Grant Agreement No. 101052200—EUROfusion) and also with support from the EPSRC [Grant No. EP/W006839/1] and the US DoE Grant Nos. DE-SC0019005, DE-SC0019007 and DE-AC05-00OR22725. Views and opinions expressed are however those of the author(s) only and do not necessarily reflect those of the European Union or the European Commission. Neither the European Union nor the European Commission can be held responsible for them. This work was partially funded by the Academy of Finland Project Nos. 324759, 328874 and 353370.

Appendix. Details about the bolometer simulations

This appendix contains the precise results and additional details of the ASCOT simulations of beam particles being neutralized by CX and hitting the bolometer foils in MAST-U. Table A1 shows the number of markers that hit each foil in each case as well as the corresponding power load. The same power-load data are shown in figure 12, where they are compared to measurements.

The simulation results when the neutral density was based on the measured neutral pressure were inspected more closely

Table A1. Number of markers that hit each counter-beam bolometer channel ('hits') and resulting estimated power load density ('power', Wm^{-2}) in each simulation case. Cases are specified by discharge number, time point during discharge (s) and whether the measured neutral pressure ('$\times p_0$' = '1') was used when reconstructing the neutral background or half ('0.5') or double ('2') the measured pressure.

channel			29		30		31		32	
discharge	time (s)	$\times p_0$	hits	power	hits	power	hits	power	hits	power
46 735	0.26	0.5	16	539.2	16	434.0	0	0.0	0	0.0
		1	30	1048.7	16	664.8	0	0.0	0	0.0
		2	42	1472.6	29	1008.1	1	11.1	0	0.0
	0.38	0.5	70	2797.6	78	2966.3	5	160.7	1	26.3
		1	106	4244.9	86	3192.8	6	125.9	1	7.1
		2	131	6352.8	109	4625.6	7	196.2	0	0.0
49 447	0.46	0.5	15	466.7	7	234.7	0	0.0	0	0.0
		1	17	627.8	15	677.7	1	12.8	0	0.0
		2	29	921.5	22	807.9	1	48.9	0	0.0
	0.58	0.5	77	2927.9	87	3368.1	4	88.0	0	0.0
		1	108	4928.7	77	3134.4	12	386.8	2	76.5
		2	126	5830.5	94	3814.9	5	148.6	2	92.9
49 452	0.36	0.5	12	322.4	9	307.7	0	0.0	0	0.0
		1	16	473.4	16	464.8	0	0.0	1	29.3
		2	41	1351.7	32	1017.5	4	103.9	0	0.0
	0.48	0.5	89	3528.0	53	2086.8	7	235.2	2	34.0
		1	84	4002.3	59	2067.5	4	102.6	2	71.3
		2	110	4979.9	86	3571.0	8	250.6	2	57.6

regarding the initial ρ_p-coordinate and final energy of those markers that hit bolometer foils. During HFS fuelling in each discharge, channels 29 and 30 were predominantly hit by markers that had originally been ionized radially further out, i.e. from the outer half of the beam-ion population. During LFS fuelling, channels 29 and 30 were hit by markers from all initial ρ_p-coordinates roughly in proportion to the birth distribution. The full energy spectrum was consistently represented among the markers that hit bolometer foils both during HFS and during LFS fuelling. However, during LFS fuelling, channels 29 and 30 were hit relatively more by markers with higher energies. This complements the preceding observation that LFS fuelling resulted in marker hits also from deeper in the plasma, since such CX neutrals must penetrate more plasma without being reionized, which requires higher energies.

The extra simulations from the sensitivity scan, performed with respect to the neutral density, shed some light on the role of statistical noise in the results. For example, it appears that the simulated power load on channel 29 in discharge 49 452 during HFS fuelling, when using the measured neutral pressure, happens to be at the low end of what the simulation might yield (figure 12(a)). A rerun with different random seeds would likely yield a power load closer to the midpoint between the power loads simulated for the half and double neutral pressures in the same plasma case. Assuming Poisson noise, where the error is the square root of the number of hits, the 'true' number of hits when using half, measured and double neutral pressure could be 9, 20 and 35, respectively, rather than 12, 16 and 41, as quoted in table A1. Because 20-million-marker simulations are computationally intensive, it was not deemed appropriate to rerun exactly the same simulations just to get several statistical samples for each result. The results obtained from the 18 simulations that were run already provide a clear enough picture.

ORCID iDs

P Ollus https://orcid.org/0000-0003-2558-1457
J Lovell https://orcid.org/0000-0001-9565-3466
K G McClements https://orcid.org/0000-0002-5162-509X
C A Michael https://orcid.org/0000-0003-1804-870X
A Snicker https://orcid.org/0000-0001-9604-9666

References

[1] Heidbrink W W and Sadler G J 1994 The behaviour of fast ions in tokamak experiments *Nucl. Fusion* **34** 535
[2] Akers R J *et al* 2002 Neutral beam heating in the START spherical tokamak *Nucl. Fusion* **42** 122
[3] Tournianski M R, Akers R J, Carolan P G and Keeling D L 2005 Anisotropic fast neutral particle spectra in the MAST spherical tokamak *Plasma Phys. Control. Fusion* **47** 671
[4] Bakharev N N *et al* 2015 Fast particle behaviour in the Globus-M spherical tokamak *Nucl. Fusion* **55** 043023
[5] Clauser C F and Farengo R 2015 Alpha particles diffusion due to charge changes *Phys. Plasmas* **22** 122502
[6] Clauser C F and Farengo R 2017 The effect of inelastic collisions on the transport of alpha particles in ITER-like plasmas *Nucl. Fusion* **57** 046013
[7] McClements K G, Tani K, Akers R J, Liu Y Q, Shinohara K, Tsutsui H and Tsuji-Iio S 2018 The effects of resonant magnetic perturbations and charge-exchange reactions on fast ion confinement and neutron emission in the Mega

Amp Spherical tokamak *Plasma Phys. Control. Fusion* **60** 095005
[8] Kramer G, Van Zeeland M and Bortolon A 2020 Full-orbit simulations of fast-ion charge-exchange losses induced by neutral particles outside the last-closed flux surface *Nucl. Fusion* **60** 086016
[9] Jaulmes F, Zadvitskiy G, Bogar K, Imrisek M, Hromadka J, Cats S Y, Varju J, Komm M and Panek R 2021 Modelling of charge-exchange induced NBI losses in the COMPASS upgrade tokamak *Nucl. Fusion* **61** 046012
[10] Ollus P *et al* 2022 Simulating the impact of charge exchange on beam ions in MAST-U *Plasma Phys. Control. Fusion* **64** 035014
[11] Mulas S *et al* 2023 Validating neutral-beam current drive simulations in the TJ-II stellarator *Nucl. Fusion* **63** 066026
[12] Xu Y, Wang F, Li Y and Zhong F 2023 Guiding-centre orbit-following simulations of charge exchange loss of NBI ions with the finite Larmor radius effect *J. Plasma Phys.* **89** 905890601
[13] Ollus P *et al* 2024 Validating the simulation of beam-ion charge exchange in MAST upgrade *Plasma Phys. Control. Fusion* **66** 025009
[14] Kiviniemi T P, Kurki-Suonio T, Lazerson S A, Äkäslompolo S J, Ollus P, Sanchis L and Kulla D 2025 The role of SOL plasma in the confinement of NBI fast ions in W7-X *Plasma Phys. Control. Fusion* **67** 025034
[15] Lovell J, Reinke M L, Field A R and Lomanowski B A (MAST Upgrade Team) 2023 Overview and first measurements of the MAST Upgrade bolometer diagnostic *Rev. Sci. Instrum.* **94** 023509
[16] Lovell J *et al* 2024 Experimental investigation of steady state power balance in double null and single null H mode plasmas in MAST Upgrade *Nucl. Mater. Energy* **41** 101779
[17] Matthews G F *et al* 2017 Energy balance in JET *Nuclear Materials and Energy* **12** 227–33
[18] Rivero-Rodriguez J F *et al* 2024 Overview of fast particle experiments in the first MAST upgrade experimental campaigns *Nucl. Fusion* **64** 086025
[19] Michael C A *et al* 2013 Dual view FIDA measurements on MAST *Plasma Phys. Control. Fusion* **55** 095007
[20] Jackson A R, Jacobsen A S, McClements K G, Michael C A and Cecconello M 2020 Diagnosing fast ion redistribution due to sawtooth instabilities using fast ion deuterium-α spectroscopy in the mega amp spherical tokamak *Nucl. Fusion* **60** 126035
[21] Prechel G, *et al* 2022 Installation of a solid state neutral particle analyzer array on mega ampere spherical tokamak upgrade *Rev. Sci. Instrum.* **93** 113517
[22] Vincent C, Allan S, Naylor G, Stephen R, Bray S, Thornton A and Kirk A 2022 Fission chamber data acquisition system for neutron flux measurements on the Mega-Amp spherical tokamak upgrade *Rev. Sci. Instrum.* **93** 093509
[23] Cecconello M *et al* 2023 First observations of confined fast ions in MAST upgrade with an upgraded neutron camera *Plasma Phys. Control. Fusion* **65** 035013
[24] Pankin A, McCune D, Andre R, Bateman G and Kritz A 2004 The tokamak Monte Carlo fast ion module NUBEAM in the national transport code collaboration library *Comput. Phys. Commun.* **159** 157–84
[25] Goldston R J, McCune D C, Towner H H, Davis S L, Hawryluk R J and Schmidt G L 1981 New techniques for calculating heat and particle source rates due to neutral beam injection in axisymmetric tokamaks *J. Comput. Phys.* **43** 61–78
[26] Varje J, Särkimäki K Kontula J Ollus P Kurki-Suonio T Snicker A Hirvijoki E and Äkäslompolo S 2019 High-performance orbit-following code ASCOT5 for Monte Carlo simulations in fusion plasmas (arXiv:1908.02482)
[27] ASCOT5. GitHub Commit 6e7cc54 with cherry-pick 58d3936 (available at: https://github.com/ascot4fusion/ascot5)
[28] Hirvijoki E, Asunta O, Koskela T, Kurki-Suonio T, Miettunen J, Sipilä S, Snicker A and Äkäslompolo S 2014 ASCOT: solving the kinetic equation of minority particle species in tokamak plasmas *Comput. Phys. Commun.* **185** 1310–21
[29] Hole M J, Appel L C and Martin R 2009 A high resolution Mirnov array for the Mega Ampere spherical tokamak *Rev. Sci. Instrum.* **80** 123507
[30] Derks G L *et al* 2024 Development of real-time density feedback control on MAST-U in L-mode *Fusion Eng. Des.* **202** 114387
[31] Militello F *et al* 2016 Characterisation of the L-mode scrape off layer in MAST: decay lengths *Nucl. Fusion* **56** 016006
[32] Scannell R, Walsh M J, Dunstan M R, Figueiredo J, Naylor G, O'Gorman T, Shibaev S, Gibson K J and Wilson H 2010 A 130 point Nd: YAG Thomson scattering diagnostic on MAST *Rev. Sci. Instrum.* **81** 10D520
[33] Rhodes T L, *et al* 2022 Design elements and first data from a new Doppler backscattering system on the MAST-U spherical tokamak *Rev. Sci. Instrum.* **93** 113549
[34] Hillesheim J C *et al* 2015 Doppler backscattering for spherical tokamaks and measurement of high-k density fluctuation wavenumber spectrum in MAST *Nucl. Fusion* **55** 073024
[35] Field A R, McCone J, Conway N J, Dunstan M, Newton S and Wisse M 2009 Comparison of measured poloidal rotation in MAST spherical tokamak plasmas with neo-classical predictions *Plasma Phys. Control. Fusion* **51** 105002
[36] McClements K G and Thyagaraja A 2006 Collective electric field effects on the confinement of fast ions in tokamaks *Phys. Plasmas* **13** 042503
[37] Boivin R L *et al* 2000 Effects of neutral particles on edge dynamics in Alcator C-Mod plasmas *Phys. Plasmas* **7** 1919–26
[38] Carreras B A, Owen L W, Maingi R, Mioduszewski P K, Carlstrom T N and Groebner R J 1998 Effect of edge neutrals on the low-to-high confinement transition threshold in the DIII-D tokamak *Phys. Plasmas* **5** 2623–36
[39] Colchin R J, Maingi R, Fenstermacher M E, Carlstrom T N, Isler R C, Owen L W and Groebner R J 2000 Measurement of neutral density near the X point in the DIII-D tokamak *Nucl. Fusion* **40** 175
[40] Viezzer E *et al* 2011 Investigation of passive edge emission in charge exchange spectra at the ASDEX Upgrade tokamak *Plasma Phys. Control. Fusion* **53** 035002
[41] Stotler D P, Scotti F, Bell R E, Diallo A, LeBlanc B P, Podestà M, Roquemore A L and Ross P W 2015 Midplane neutral density profiles in the National Spherical Torus Experiment *Phys. Plasmas* **22** 082506
[42] Scotti F, Stotler D P, Bell R E, LeBlanc B P, Sabbagh S A, Soukhanovskii V A, Umansky M V and Zweben S J 2021 Outer midplane neutral density measurements and H-mode fueling studies in NSTX-U *Nucl. Fusion* **61** 036002
[43] Havlíčková E, Harrison J, Lipschultz B, Fishpool G, Kirk A, Thornton A, Wischmeier M, Elmore S and Allan S 2015 SOLPS analysis of the MAST-U divertor with the effect of heating power and pumping on the access to detachment in the Super-x configuration *Plasma Phys. Control. Fusion* **57** 115001
[44] Conway N J, Carolan P G, Mccone J, Walsh M J and Wisse M 2006 High-throughput charge exchange recombination spectroscopy system on MAST *Rev. Sci. Instrum.* **77** 10F131
[45] ITER Physics Expert Group on Confinement and Transport, ITER Physics Expert Group on Confinement Modelling and Database and ITER Physics Basis Editors 1999 Chapter 2: Plasma confinement and transport *Nucl. Fusion* **39** 2175

[46] Dudson B D *et al* 2008 Experiments and simulation of edge turbulence and filaments in MAST *Plasma Phys. Control. Fusion* **50** 124012
[47] Asunta O, *et al* 2015 Modelling neutral beams in fusion devices: beamlet-based model for fast particle simulations *Comput. Phys. Commun.* **188** 33–46
[48] LaBombard B 2001 KN1D: a 1-D space, 2-D velocity, kinetic transport algorithm for atomic and molecular hydrogen in an ionizing plasma (available at:https://dspace.mit.edu/handle/1721.1/93211)
[49] Johnson L C and Hinnov E J 1973 Ionization, recombination and population of excited levels in hydrogen plasmas *J. Quant. Spectrosc. Radiat. Transfer* **13** 333
[50] Bowman C 2022 *Pedestal-inference version 0.3.0* (available at:https://github.com/C-bowman/pedestal-inference)
[51] Janev R K, Reiter D and Samm U 2003 *Collision Processes in Low-temperature Hydrogen Plasmas* (Forschungszentrum Jülich, Zentralbibliothek)
[52] Lao L L, John H S, Stambaugh R D, Kellman A G and Pfeiffer W 1985 Reconstruction of current profile parameters and plasma shapes in tokamaks *Nucl. Fusion* **25** 1611
[53] Appel L C *et al* 2006 A unified approach to equilibrium reconstruction *Proc. 33rd EPS Conf. on Controlled Fusion and Plasma Physics* p –2.160
[54] Summers H P, Dickson W J, O'mullane M G, Badnell N R, Whiteford A D, Brooks D H, Lang J, Loch S D and Griffin D C 2006 Ionization state, excited populations and emission of impurities in dynamic finite density plasmas: I. the generalized collisional–radiative model for light elements *Plasma Phys. Control. Fusion* **48** 263
[55] Ollus P 2025 Charge-exchange losses of beam ions in MAST Upgrade: experiments and modelling (Version 1.0) [Data set] United Kingdom Atomic Energy Authority (UKAEA) (https://doi.org/10.14468/h59b-p097)